

Red Dots: A temperate 1.5 Earth-mass planet in a compact multi-terrestrial planet system around GJ 1061[★]

S. Dreizler,^{1†} S. V. Jeffers¹, E. Rodríguez², M. Zechmeister¹, J. R. Barnes³, C. A. Haswell³, G. Coleman⁴, S. Lalitha¹, D. Hidalgo Soto⁵, J. B. P. Strachan⁶, F.-J. Hamsch⁷, M. J. López-González², N. Morales², C. Rodríguez López², Z. M. Berdiñas⁸, I. Ribas^{9,10}, E. Pallé^{5,11}, A. Reiners¹, and G. Anglada-Escudé^{6,2},

¹*Institut für Astrophysik, Georg-August-Universität, Friedrich-Hund-Platz 1, 37077 Göttingen, Germany*

²*Instituto de Astrofísica de Andalucía (IAA-CSIC), Glorieta de la Astronomía s/n, 18008 Granada, Spain*

³*School of Physical Sciences, The Open University, Walton Hall, Milton Keynes, MK7 6AA, UK*

⁴*Universität Bern, Physikalisches Institut, Universität Bern, Gesellschaftsstr. 6, 3012 Bern, Switzerland*

⁵*Instituto de Astrofísica de Canarias (IAC), Vía Láctea s/n, 38205 La Laguna, Tenerife, Spain*

⁶*School of Physics and Astronomy, Queen Mary, University of London, 327 Mile End Road, London, E1 4NS*

⁷*Vereniging Voor Sterrenkunde, Brugge, Belgium*

⁸*Departamento de Astronomía, Universidad de Chile, Camino El Observatorio 1515, Las Condes, Santiago, Chile*

⁹*Institut de Ciències de l'Espai (ICE, CSIC), Campus UAB, C/Can Magrans s/n, 08193 Bellaterra, Spain*

¹⁰*Institut d'Estudis Espacials de Catalunya (IEEC), 08034 Barcelona, Spain*

¹¹*Departamento de Astrofísica, Universidad de La Laguna (ULL), 38206 La Laguna, Tenerife, Spain*

Accepted XXX. Received YYY; in original form ZZZ

ABSTRACT

Small low-mass stars are favourable targets for the detection of rocky habitable planets. In particular, planetary systems in the solar neighbourhood are interesting and suitable for precise characterisation. The Red Dots campaigns seek to discover rocky planets orbiting nearby low-mass stars. The 2018 campaign targeted GJ 1061, which is the 20th nearest star to the Sun. For three consecutive months we obtained nightly, high-precision radial velocity measurements with the HARPS spectrograph. We analysed these data together with archival HARPS data. We report the detection of three planet candidates with periods of 3.204 ± 0.001 , 6.689 ± 0.005 and 13.03 ± 0.03 days, which is close to 1:2:4 period commensurability. After several considerations related to the properties of the noise and sampling, we conclude that a 4th signal is most likely explained by stellar rotation, although it may be due to a planet. The proposed three-planet system (and the potential four-planet solution) is long-term dynamically stable. Planet-planet gravitational interactions are below our current detection threshold. The minimum masses of the three planets range from 1.4 ± 0.2 to $1.8 \pm 0.3 M_{\oplus}$. Planet d, with $m \sin i = 1.68 \pm 0.25 M_{\oplus}$, receives a similar amount of energy as Earth receives from the Sun. Consequently it lies within the liquid-water habitable zone of the star and has a similar equilibrium temperature to Earth. GJ 1061 has very similar properties to Proxima Centauri but activity indices point to lower levels of stellar activity.

Key words: methods: data analysis – planetary systems – stars: late-type – stars: individual: GJ 1061

1 INTRODUCTION

The Red Dots collaboration¹ is an effort to detect exoplanets orbiting our nearest stellar neighbours, i.e., stars within 5 pc, by concentrating the observational efforts on one star

[★] This research has made use of the services of the ESO Science Archive Facility. Based on observations collected at the European Southern Observatory under ESO programmes 072.C-0488(E), 183.C-0437(A), 0101.C-0516(A), and 198.C-0838(A).

† E-mail: dreizler@astro.physik.uni-goettingen.de

¹ <https://reddots.space/goals/>

at a time. The Red Dots observing cadence ensures the good sampling of signals only partially constrained from previous campaigns. This strategy was decisive in the discovery of Proxima b, orbiting our closest stellar neighbour Proxima Centauri (Anglada-Escudé et al. 2016); it contributed significantly to the discovery of Barnard’s Star b (Ribas et al. 2018), and revealed the paucity of terrestrial planet candidates in Barnard’s Star.

Within 5pc, there are 15 exoplanet systems known, mostly around M-stars. Three of them are high multiplicity systems: YZ Ceti (Astudillo-Defru et al. 2017c), Wolf 1061 (Wright et al. 2016; Astudillo-Defru et al. 2017b), and GJ 876 (Rivera et al. 2010). For planetary systems around low-mass stars similar to our target GJ 1061 (a late type M-star with low mass of $M = 0.12 M_{\odot}$), state-of-the-art planet formation simulations show that planets form outside the water ice-line. They migrate into warm orbits close to the central star when they attain masses of $0.5\text{--}1 M_{\oplus}$ (Coleman et al. 2017; Alibert & Benz 2017). Typically, these planets migrate in resonant chains and continue to accrete solid material. This means that multi-planet systems of hot and warm Earth-mass and super-Earth planets is a common outcome, with the majority of these systems remaining in or close to resonant configurations. Observed planetary systems around stars similar to GJ 1061, such as YZ Ceti, Proxima, TRAPPIST-1 (Gillon et al. 2017; Grimm et al. 2018), as well as Teegarden’s star (Zechmeister et al. 2019) closely match the simulations from recent work which uses both pebble and planetesimal accretion scenarios to form the planetary systems (Coleman et al. 2019).

While other programmes such as HIRES/Keck (Butler et al. 2017) or the HARPS survey (e.g. Astudillo-Defru et al. 2017c) have detected numerous planets by working on large samples of stars, our strategy is different. We perform uniform, nightly cadence spectroscopic and photometric monitoring of a very small number of targets (up to three per season) to cover the periods of temperate orbits several times in each season (up to three months). This strategy has proven optimal (Anglada-Escudé et al. 2016) for detection of low-mass planets in hot to temperate orbits around nearby red-dwarfs, and for identifying and mitigating intrinsic stellar variability and spurious correlations as also demonstrated by Damasso & Del Sordo (2017).

In this paper we first introduce GJ 1061 with its basic stellar parameters (Sect. 2) followed by a presentation of the spectroscopic and photometric data (Sect. 3). In the analysis (Sect. 4), we first describe the signal detection in the radial velocity data and the detailed analysis of the signals (4.1). In order to assess their origin being due to planetary orbits or stellar activity we then analyse the spectroscopic activity indices and the photometry (4.2). The results are finally discussed in Sect. 5.

2 GJ 1061

2.1 General properties of GJ 1061

The stellar parameters, including activity indices, are summarised in Table 1. At a distance of ~ 3.67 pc (Gaia Collaboration et al. 2018), GJ 1061 is the 20th nearest star to the

Table 1. Stellar parameters for GJ 1061.

Parameter	Value	Ref.
Alias name	L 372-58	
α	03 35 59.700	<i>Gaia</i>
δ	−44 30 45.725	<i>Gaia</i>
$\mu_{\alpha} \cos \delta$ [mas/yr]	745.286 ± 0.118	<i>Gaia</i>
μ_{δ} [mas/yr]	-373.673 ± 0.138	<i>Gaia</i>
π [mas]	272.2446 ± 0.0661	<i>Gaia</i>
V [mag]	13.06 ± 0.07	G14
J [mag]	7.523 ± 0.02	2MASS
Sp. type	M5.5V	H02
T_{eff} [K]	$2953 \pm 98, 2999 \pm 41$	S18, G14
L [$10^{-3} L_{\odot}$]	$1.7 \pm 0.1, 3$	S18, G14
R [R_{\odot}]	$0.156 \pm 0.005, 0.19$	S18, G14
M [M_{\odot}]	$0.12 \pm 0.01, 0.14$	S18, G14
[Fe/H] [dex]	-0.08 ± 0.08	N14
γ [km/s]	1.06 ± 0.01	this work
$v \sin i$ [km/s]	< 2.5	this work
$\log L_{\text{H}\alpha} / L_{\text{bol}}^*$	< 4.88 (inactive)	this work
$\log L_{\text{X}} / 10^{-7} \text{ W}$	26.07	S04
Age [Gyr]	$> 7.0 \pm 0.5$	W08

Notes. *: see Jeffers et al. (2018a) for a conversion from equivalent width to the luminosity ratio as well as for the threshold for inactive stars.

References. *Gaia*: Gaia Collaboration et al. (2018); G14: Gaidos et al. (2014); 2MASS: Skrutskie et al. (2006); H02: Henry et al. (2002); S18: Stassun et al. (2018); N14: Neves et al. (2014); R74: Rodgers & Eggen (1974); B14: Barnes et al. (2014); S04: Schmitt & Liefke (2004); W08: West et al. (2008).

Sun² and has an effective temperature T_{eff} slightly below 3000 K (Gaidos et al. 2014; Stassun et al. 2018). Two different T_{eff} values are reported by Stassun et al. (2018) and Gaidos et al. (2014). While both are consistent, the stellar radius, luminosity, and mass differ between both studies. Since this affects the derived planetary parameters we explicitly indicate in Sect. 4 and 5 which parameters were used.

2.2 Activity, age, and rotation period estimates

Mid-M dwarf stars generally show significant magnetic activity (e.g., West et al. 2008; Reiners et al. 2012; Barnes et al. 2014; Jeffers et al. 2018b, and references therein). GJ 1061 is relatively magnetically inactive with little or no signs of H α emission (Barnes et al. 2014) and a so far undetermined rotation rate. Schmitt & Liefke (2004) reported a very low detection of X-ray emission at the level of $\log L_{\text{X}} \sim 26.07$. Given its very low activity GJ 1061 has been used by Barnes et al. (2017) as a slowly rotating inactive reference for Doppler imaging studies.

The chromospheric Ca II index of GJ 1061 is one of the lowest ($\log R'_{\text{HK}} = -5.32$) among several thousand stars investigated by Boro Saikia et al. (2018, see Fig. 3). This is in agreement with the value $\log R'_{\text{HK}} = -5.754$ obtained by Astudillo-Defru et al. (2017a). These $\log R'_{\text{HK}}$ values suggest a rotation period ranging from 50 to 130 days accord-

² <http://www.recons.org/>

ing to the relations by Suárez Mascareño et al. (2015) and Astudillo-Defru et al. (2017a) and are consistent with the inferred rotation period in the range of 50–200 d from the X-ray activity-rotation relation by Pizzolato et al. (2003), Wright et al. (2011), and Reiners et al. (2014). These ranges of potential rotation period are consistent with the absence of H α emission (Newton et al. 2017) and is consistent with $v \sin i < 5 \text{ km s}^{-1}$ reported by Barnes et al. (2014) who as well reported $-6.74 \leq \log L_{\text{H}\alpha}/L_{\text{bol}} \leq 6.12$ and very low amplitude activity. From the lack of H α emission we can infer that the star is older than the so-called activity lifetime of an M5 or M6 dwarf, which is $7.0 \pm 0.5 \text{ Gyr}$ (West et al. 2008). Neither circumstellar material nor stellar multiplicity has been detected for GJ 1061 (Avenhaus et al. 2012; Rodríguez et al. 2015) using the WISE and HERSCHEL satellite. Thus, though the star’s bulk properties are very similar to those of Proxima Centauri (Anglada-Escudé et al. 2016), GJ 1061 seems to be less active. These findings are further supported by the pilot precision radial velocity survey of a sample of 15 M5V - M9V stars conducted over a six night span by Barnes et al. (2014); GJ 1061 showed the lowest variability with r.m.s. variability $< 5 \text{ ms}^{-1}$.

3 OBSERVATIONS

3.1 HARPS Red Dots

Observations during 54 nights were made using the HARPS spectrograph at the ESO 3.6 m at La Silla (Mayor et al. 2003) from July to September 2018 with exposure times of 1800 s and an average signal-to-noise ratio of ~ 20 at 650 nm. We also analyse public archival data (*HARPS public*³) treating the seven pre-fiber upgrade and 107 post-fiber upgrade data as separate sets (Lo Curto et al. 2015). All reduced spectra were processed with both TERRA (Anglada-Escudé & Butler 2012) and SERVAL (Zechmeister et al. 2018) codes, yielding radial velocities (RVs), pseudo equivalent widths (pEW) of H α and Na I D, and differential line widths (dLW, see Sect. 3.2 of Zechmeister et al.). We use nightly averages in cases of multiple exposures per night resulting in 98 post-upgrade measurements.

3.2 Photometry

Contemporaneous photometry from ASH2⁴, MONET-South⁵, and AAVSO⁶ was obtained to determine the stellar rotation period of GJ 1061. Moreover, the TESS mission (Ricker et al. 2015b) observed this target in continuous mode for ~ 50 consecutive days during our Red Dots campaign. We also used archival photometry from MEarth (Berta et al. 2012) and ASAS-SN (Kochanek et al. 2017). These data sets are summarised in Table 2. The corresponding observing facilities are described in Appendix E and Table E1, the photometric data are listed in Table E2.

All new ground-based CCD measurements were obtained by the method of synthetic aperture photometry.

³ ESO programme 198.C-0838(A), PI Bonfils

⁴ Astrograph for South Hemisphere II

⁵ MONitoring NETWORK of Telescopes

⁶ American Association of Variable Star Observers

Table 2. Properties of the photometric data sets^a

Data set	Season	ΔT [d]	N_{obs}	N_n	rms [mmag]
ASH2 V	2018	97	426	32	6.8
ASH2 R	2018	97	426	32	8.6
MONET-S	2018	96	4320	43	21.2
AAVSO	2018	123	6987	103	11.8
TESS	2018	53	27602	44	1.5
MEarth T11	2017	92	1031	31	10.1
MEarth T13	2016/17	243	10607	171	8.8
ASAS-SN	2014/18	1558	1054	407	60.5

Notes. ^a Data set identifier, season, time span, number of individual observations, number of nights and rms as average uncertainty over all nights in each data set.

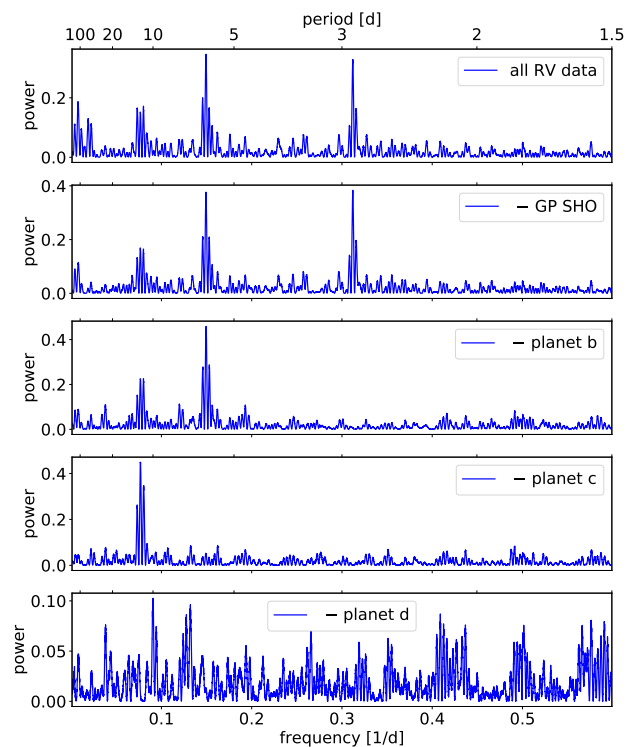


Figure 1. *Top:* Periodograms of HARPS pre-, post-upgrade data with consecutively removed signals. The periodograms of the individual signals are shown in the Appendix in Fig. D1.

Each CCD frame was corrected in a standard way for bias and/or dark, and flat field by instrument specific pipelines. From a number of nearby and relatively bright stars within the frames, the best sets were selected as reference stars.

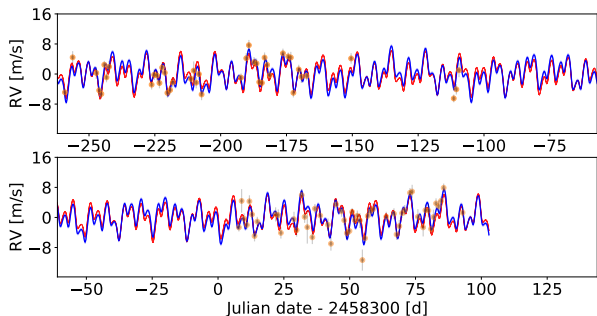


Figure 2. HARPS public and Red Dots data (from BJD 2458300 on) measurements with our favoured model with 3-planet model (red). The blue line includes the modeling of the correlated noise using the *SHO* kernel from *celerite*.

4 DATA ANALYSIS

4.1 Signal detection in the radial velocities, and model parameters

The RV analysis incorporates all measurements listed in Tables A1 and A2, except for one outlier⁷. The first step of the analysis is to detect the most likely periodic signals in the data and assess their significance using likelihood periodograms (Baluev 2009). We use an iterative sequential procedure consisting of: i) computing a likelihood periodogram to identify the period of the (next) most probable signal, ii) including the signal in the model and repeating the process until no significant signals remain. Using our favoured model described below, this procedure is illustrated in Fig. 1, showing four detected signals. Sometimes a new period is significant, but ambiguous due to aliasing. To ensure a secure and unique period determination, we additionally require that the maximum likelihood solution (highest peak) must have a $\Delta \ln L > 5$ compared to the second highest peak. In a Bayesian sense, this is equivalent to requiring that the model probability (assuming uniform priors) of the best solution must be $e^5 \sim 150$ times more probable than any other solution with an alternative period and the same number of parameters. In addition to Keplerian signals, the model also includes a zero-point offset and a white noise jitter parameter for each set, a global linear trend, and a model for the correlated noise (see below). We also used the *Systemic* (Meschiari et al. 2009) interface to visually verify that the solution was indeed unique.

In the second step, i.e. the detailed analysis, we deployed a python script using *celerite* (Foreman-Mackey et al. 2017) and *emcee* (Foreman-Mackey et al. 2013) to characterize the credibility intervals for all the parameters in the model. For an increasing number of planets ($N = 0, 1, 2, 3, 4$) the parameters for each Keplerian model are the orbital period P , the radial velocity semi-amplitude K , the eccentricity e , the periastron longitude ω as well as the periastron passage time t_{peri} ⁸. The 4th signal was alternatively modelled using

the stochastically driven damped harmonic oscillator kernel (*SHO*) provided by *celerite* to account for correlations between data points using a Gaussian Process (GP) framework (see Appendix B for more details). Model parameters for this kernel are an amplitude S_0 , a resonance frequency ω_0 (we convert it in a period P_0), and the quality factor Q of the oscillator converted to a damping time scale, τ_d . Like in the first step, the model also includes a zero-point offset and a white noise jitter parameter⁹ for each instrument, and a global linear trend.

The first and second signals (planets b and c) are unique with no severe aliasing ambiguities. However, for the third signal (planet d), the period could be either 13.0 d or 12.4 d given that the $\Delta \ln L$ between the two solutions is only about 2.5. In frequency space, the difference between $1/13.0 \text{ d}^{-1}$ and $1/12.4 \text{ d}^{-1}$ is $1/270$, which corresponds to the highest secondary lobe of the window function for this time series, thus the confusion is probably caused by aliasing. The bulk properties of the planet candidates (period and mean longitude) do not change dramatically between solutions but the amplitude and therefore mass is affected, although within error bars. Further observations can pin-down the precise period and orbital elements. Both solutions are listed in Table 3.

A similar, but more problematic, situation occurs with the 4th signal. From the periodograms we cannot robustly distinguish between $P=53 \text{ d}$ and $P=130 \text{ d}$ because these two solutions only differ by a $\Delta \ln L$ of ~ 3 ; including either in the model removes the other, indicating an aliasing between the two. Treating the 4th signal as a Keplerian orbit results in a rather high eccentricity of $e=0.34$. When modelled with the *SHO*-kernel, the fit favours a period of $P_0 = 53 \text{ d}$ rather than 130 d and an unconstrained long damping time $\tau_d > 130 \text{ d}$. Since the period of the 4th signal is overlapping with the probable range for the rotation period, we discuss the interpretation of that signal as due to activity or planetary orbit in Section 4.2.

We also tested whether a $N = 4$ model with $P_4 = 53 \text{ d}$ including an *SHO* kernel would result in a statistically significantly better fit. This is not the case since the log-likelihood increases only by 3. By comparison of the log-likelihood of the different models ($N = 0 \dots 4$, *SHO*) and taking potential activity induced RV signals into consideration (see below) we identified our favoured model as the one with three planets and a *SHO* kernel to describe the correlated noise.

Table 3 summarizes the most probable parameter values, their credibility intervals, and the statistical significance of each signal for our favoured model with three Keplerian signals and the *SHO* kernel. The improvement of the fit compared to $N - 1$ signals is indicated as $\Delta \ln L$. Statistical significances are given through the False Alarm Probability estimates derived from the improvement in the log-likelihood statistic (Baluev 2009). Fig. 2 shows the best fit for all post-upgrade HARPS data. Fig. 3 shows the final phase-folding

Allowing eccentric Keplerian solutions for them does not significantly improve upon circular orbit fits.

⁹ The jitter parameter for the HARPS pre-upgrade data result in an unrealistic high value of about 10 m/s which is likely due to the fact that this data set only contains seven data points scattered over about 10 years. We therefore fixed this jitter parameter to 1 m/s. This has no impact on the overall results.

⁷ The excluded RV point is a 5.5σ outlier from JD=2458376.8825. The spectrum shows no anomaly except the +20.45 m/s RV deviation. It is listed in Table A2 for completeness.

⁸ The eccentricities of the first three Keplerian signals are small.

with the model specified in Table 3. The periodograms of the data with these four signals subsequently removed are shown in Fig. 1, the periodograms of the corresponding models are shown in Fig. D1. The posterior distribution of the parameters are shown in the Appendix in Figs. C1 to C3.

As a final check, we investigated the phase coherence using data from 2017 (HARPS public) and 2018 (HARPS Red Dots) separately. The first three signals are detected in both sub-sets with parameters matching the full analysis, however, larger uncertainties (about factor 10 in period and factor 2 in mass). Neither season is sufficiently long for a clear detection of the fourth signal. This is further illustrated with Fig. D2 in Appendix D. The signals from the three planets are coherent over two seasons, i.e. these detections are robust.

4.2 Activity or planets?

After the signal detection, we assess the validity of the interpretation of the signal as being due to planetary orbits or due to stellar activity. We employ spectroscopic activity indices as well as photometry in the following.

4.2.1 Spectroscopic indices

We measured pseudo-equivalent widths (EW) of the two Na I D lines and H α chromospheric lines as obtained with *TERRA* (Table F1) to search for evidence of periodicities in the stellar activity (Fig. F2). For this investigation, we excluded epochs with EW measurements showing significant deviations from the quiescent state of the chromosphere of the star (occasional small flares, cosmic rays, and background contamination can all cause spurious measurements of EW) through a two-step 3σ clipping. These excluded measurements are flagged with 0 in the online version of the data tables. The H α index shows a signal at about 130 d which we can well model (Fig. F1) with a Gaussian Process using the *SHO* kernel described above.

Changes in the width of the average spectral line are known to correlate with spurious Doppler shifts. We also investigated differential change in the line width (or dLW, Table A2) from *SERVAL* (Zechmeister et al. 2018). The periodogram of this index (Fig. F4) show two possible signals at 27 d and 13.5 d, but at rather low significance (FAP \sim 1-10%). The latter is close to, but not exactly at the period of one of the RV signals, so we examined the issue further. We fitted the dLW-data with three models: a Keplerian model accounting for strictly periodic but not necessarily sinusoidal variations; and with two different kernels provided by *celerite* to model correlations between data points. The *REAL* kernel describes correlation through an exponential excitation or decay at a characteristic time scale, the *SHO* kernel is as described above (Sect. 4.1). The fit with a periodic Keplerian-like signal yields 26.07 ± 0.04 d, where the eccentricity also accounts for the signal at 13.5 d (first harmonic). However, this signal is not coherent over all data, but only for about one observing season of about 100 d length. The fit of the dLW (Fig. F3) using both kernels results very short characteristic and damping timescales (of few days), which further supports that the coherence of the signal is short lived. On the other hand, the third RV signal is

very coherent throughout the season (see colour coded phase folded plots Fig. 3), so we consider it very unlikely that the dLW and RV signals are related at a significant level. The dLW signal does not match the photometric period either (Sect. 4.2.2) but it is about half of the 53 d period present in the RV data. This raises doubt on the planetary origin of the 53 d signal.

It should be noted that the dLW may also be due to instrumental or observational effects. Even when the star is very inactive, spurious signals can arise from varying Moon contamination (periodicity close to the detected ~ 27 d), varying background and therefore spectral line contrast, or small instrumental variations such as small focus changes.

4.2.2 Photometry analysis

TESS (Ricker et al. 2015a) observed GJ 1061 in Sector 3 and 4 (TIC79611981). With the planetary radii derived in Sect. 5 we expect transit depths between about 3 and 40 mmag, depending on the planetary composition. Using the Mikulski Archive for Space Telescopes (MAST)¹⁰, we inspected the *TESS* data for transits, finding no transit signal at any of the RV periods. *TESS* data has a too short time-span (~ 60 days) for a detection of the potential long-term rotation modulation in GJ 1061.

We combined most ground-based time series (omitting ASAS-SN due to large rms and ASH2 V) that we could find on the star, including the new Red Dots photometric data obtained (quasi-)simultaneously to the HARPS observations (Fig. E1). The combined analysis using an *SHO* kernel as well as individual offsets and jitter terms shows several strong and clear signals in the range of 60–150 d (Fig. E2, top). We are aware of the fact that a combination of ground-based photometry using different filters as well as comparison stars is prone to artefacts. We therefore also investigate the data sets individually. ASH2 R as well as AAVSO show a long-term periodicity which is however unconstrained due to insufficient duration. In the MEarth T13 data set periodicity at 130 ± 5 d is seen most clearly. The 130 d signal is not coherent over the full photometric data set; this is consistent with an origin in relatively short-lived active regions on the slowly rotating stellar surface. The MEarth T13 data set also shows power in the 5 d and 2.5 d range at low amplitude. These, however, disappear in the residuals (Fig. E2, bottom).

Using the *SHO* kernel, we estimate a damping time $\tau_d \sim 20$ d, i.e. significantly shorter than the underlying oscillator period of ~ 130 d further supporting this picture. Alternatively, the *REAL* kernel yields $\tau_d \sim 44$ d. Correlation kernels following an over-damped oscillator produce signals in a broad period range as discussed in Ribas et al. (2018)¹¹.

We therefore assessed the chances of the 4th signal being a false positive induced by correlated noise with the characteristics of those of the star activity traced by the photometry. Since the period of 130 d being detectable in

¹⁰ <https://mast.stsci.edu/>

¹¹ As a word of caution we like to note that the parameters of the GP models may not have a physical meaning but due to instrumental systematics or due to the combination of inhomogeneous data like in this case.

Table 3. Model and reference statistical parameters from the simultaneous fit of HARPS pre and post upgrade data for the 3-Keplerian signals plus *SHO* model. Although we fit full Keplerian orbits, they are indistinguishable from circular ones (Fig. C2-C3). The derived values for semi-major axis and planetary mass take the stellar mass uncertainty listed in Table 1 into account. Due to aliasing, we list two solutions for planet d (solutions with $P_d = 12.4$ denoted with *). $\Delta \ln L$ indicates the fit improvement with respect to the model with one less planet. False Alarm Probabilities (FAPs) are calculated from the improvement of the log-likelihood statistic following [Baluev \(2009\)](#).

Keplerian parameters	Planet b	Planet c	Planet d	Planet d*
Detection order	#1	#2	#3	#3*
P [d]	3.204 ± 0.001	6.689 ± 0.005	$13.031^{+0.025}_{-0.032}$	$12.434^{+0.031}_{-0.023}$
K [m/s]	2.43 ± 0.24	$2.48^{+0.28}_{-0.29}$	1.86 ± 0.25	
K^* [m/s]	2.54 ± 0.25	2.39 ± 0.24		1.76 ± 0.28
e [-] ^a	< 0.31	< 0.29	< 0.53	< 0.54
ω [deg]	145^{+81}_{-65}	88^{+95}_{-85}	157^{+88}_{-71}	278^{+49}_{-214}
t_{peri} [d] ^b	$0.61^{+0.56}_{-0.72}$	$0.2^{+1.9}_{-1.5}$	$6.4^{+3.1}_{-2.5}$	$8.0^{+2.0}_{-2.4}$
Derived parameters				
a [au]	0.021 ± 0.001	0.035 ± 0.001	0.054 ± 0.001	0.052 ± 0.001
$m \sin i$ [M_{\oplus}]	$1.38^{+0.16}_{-0.15}$	1.75 ± 0.23	$1.68^{+0.25}_{-0.24}$	
$m \sin i^*$ [M_{\oplus}]	$1.44^{+0.17}_{-0.16}$	1.74 ± 0.20		$1.57^{+0.27}_{-0.25}$
λ [deg] ^{b,c}	66.0 ± 5.7	80.0 ± 7.6	$335.7^{+8.4}_{-8.0}$	72.2 ± 8.9
t_c [d] ^{b,d}	3.4 ± 0.1	6.9 ± 0.2	4.2 ± 0.7	13.1 ± 0.7
F [S_{\oplus}] ^c	3.8 ± 0.7	1.4 ± 0.2	0.6 ± 0.1	0.6 ± 0.1
HARPS pre [m/s]			1.0^d	
HARPS post & Red Dots [m/s]			$1.06^{+0.18}_{-0.17}$	
$\Delta \ln L$	16.8	19.1	23.3	
FAP [10^{-5}]	4.5	1.6	0.12	

Notes. ^a Upper limit to orbital eccentricities (99% credibility interval). ^b Reference time is BJD=2458300. ^c Mean longitude. ^d Time of inferior conjunction. ^e Insolation with stellar parameters adopted from [Stassun et al. \(2018\)](#). ^f fixed.

the RV, photometric, and H_{α} activity index data, we concentrate on the 53 d signal in the following. We generated 50 000 realisations of correlated noise using the *REAL* kernel with a $\tau_d \sim 44$ d at the sampling of the RV data. For each of those we obtained the highest peak from a GLS periodogram ([Zechmeister & Kürster 2009](#)). As expected, we find a broad distribution of periods among those peaks with a broad maximum in the range 100 to 400 d. A signal with a period of between 51 and 57 d (the full range of periods from the $N = 4$ planet fit) is found with 16% chance. For the shorter orbital periods a false-alarm probability is negligible. While a planetary origin for the 53 d signal cannot be ruled out, we consider stellar activity is the most likely explanation for this 4th signal.

Summarizing, both, the 53 d and the 130 d signal are within the expected range for the stellar rotation period as mentioned in Sect. 2.2. Both have possible counter parts in the activity indices (twice the period of the dLW) or photometry. The common detection of the 130 d signal in RV, photometric, and activity index data justify to identify the 130 d period as the stellar rotation period.

4.3 A stable compact planetary system

We tested the dynamical properties of the model using *mercury6* ([Chambers 1999](#)) and *Systemic*, and assuming four planets as the dynamically most challenging case. Consistent with expectations based on separations compared to mutual Hill radii, and the period commensurabilities (close to 1:2:4:16), the system survives at least 10^8 years. This is, however, requiring small eccentricities for planets b to d, especially planet c needs an eccentricity near zero in order to keep the system long-term stable. We found that, when adopting the minimum planet masses, the system is not in a mean-motion resonance since the libration angles rotate. Significant exchanges of angular momentum are nevertheless present and manifest as regularly oscillating eccentricities. A dynamical fit results in a very subtle shift in orbital periods within the error bars which, over the duration of observation, causes a slight phase shift without corresponding to a statistically better model. The planetary system remains stable even if viewed almost face-on, at an inclination of $i = 10^\circ$. This dynamical robustness precludes strong constraints on the system's inclination. For randomly oriented systems, geometrical arguments disfavour small values of i and thus masses larger than 3-4 times the reported minimum masses.

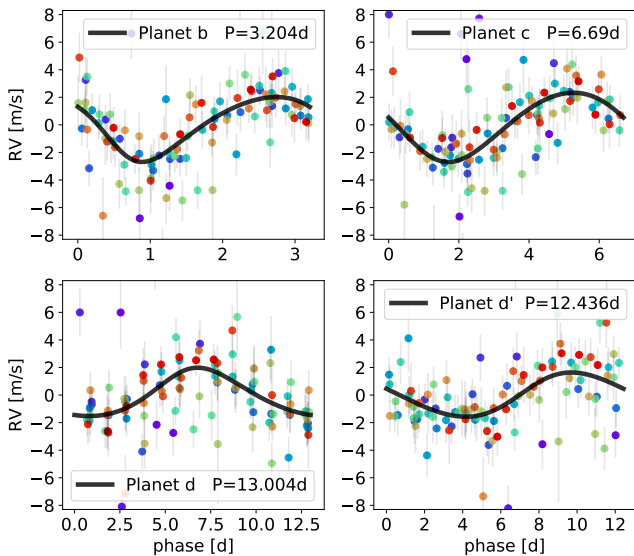


Figure 3. Phased HARPS Red Dots data for the 4-signal fit for the 3 planets. Top panels are for planets b and c, and bottom panels are for the two possible solutions for planet d with periods of 13.0 and 12.4 d. The fourth signal is modeled using the *SHO*-kernel. The color indicates the time of observation (chronological order from blue to red) to illustrate the coherence and of the signals along the campaigns.

Probabilistic arguments based on the Kepler mission’s detection statistics and comparison to RV detected samples (e.g. Bixel & Apai 2017) makes it *a priori* very unlikely that these planets have masses larger than $3 M_{\oplus}$.

5 DISCUSSION AND CONCLUSIONS

We find three RV signals that can be attributed to planets with minimum masses close to the mass of the Earth matching the expectation from state-of-the-art planet formation simulations (Coleman et al. 2017; Alibert & Benz 2017). All three signals are coherent over the observational time span ~ 1 year. A fourth signal is also significant, but considering all available data we find that it is mostly likely caused by correlated noise induced by stellar activity and rotation; we find $P_{\text{rot}} \sim 130$ d, since this signal is detected in the RV, photometric as well as H_{α} index data. Whether the signal at 53 d is only due to correlated noise or planetary origin would require longer-term observations with dense coverage over about five months in order to check its coherence as well as amplitude stability.

Using the stellar parameters (Table 1) and planetary parameters (Table 3) we show the three planets in relation to the star’s habitable zone (Fig. 4), assuming the minimum mass as the actual mass. Fig. 4 shows their insolation, that of other Earth-like planets, and the limits of the optimistic and conservative habitable zone (Kopparapu et al. 2014). The two sets of stellar parameters result in different insolation values for the planets. We propagate the uncertainties in T_{eff} into the uncertainties in insolation values. With an orbital period of around 13 d, planet d is the most interesting regarding potential habitability as it lies well within the

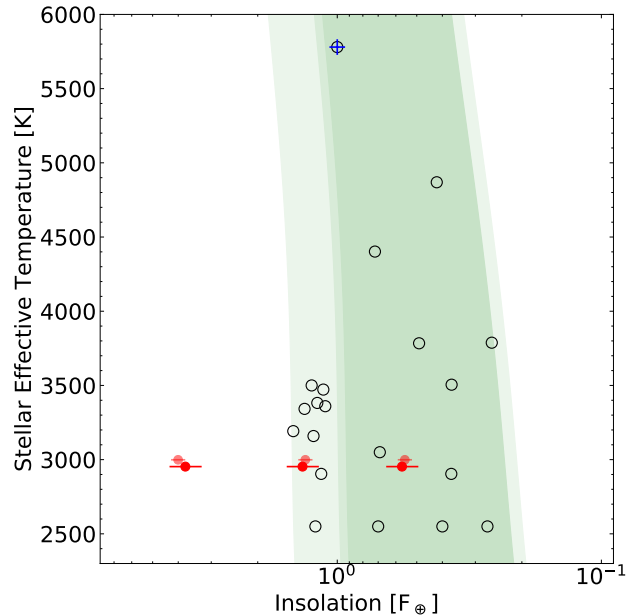


Figure 4. The optimistic (light green) and conservative (dark green) habitable zone for $1 M_{\oplus}$ according to Kopparapu et al. (2014). GJ 1061 planets b to d are shown as red dots using the stellar parameters from Stassun et al. (2018) and as light red dots using values from Gaidos et al. (2014). For comparison we plot selected planets (including Proxima b Anglada-Escudé et al. 2016, TRAPPIST-1 e, f, and g Gillon et al. 2017, Teegarden’s star b and c Zechmeister et al. 2019, and GJ 357 d Luque et al. 2019) and the Earth (black-blue circled plus) at the top.

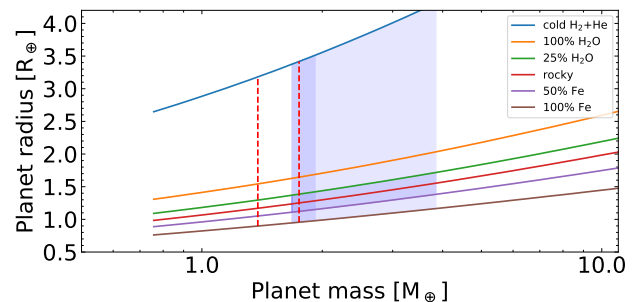


Figure 5. Mass-radius-relation for various compositions (Zeng et al. 2016). The range of masses up to 90% cumulative probability of planet d is shaded in light blue. The region of less extreme compositions between 25% H_2O and 50% Fe is additionally highlighted. Stellar parameters are taken from (Stassun et al. 2018). Additionally shown are the lower masses for the other planets (red dashed lines).

classic liquid water habitable zone for both sets of stellar parameters. The range of possible sizes for planet d are shown in Fig. 5 for various planetary composition ranging from a cold H+He to a pure Fe composition (Zeng et al. 2016).

This study illustrates the efficiency of the Red Dots observing strategy. Our homogeneously sampled data over one season has been essential to the robust detection of the three short period planets. Additional planets in longer-period or-

bits may also be present in the system. The non-zero linear trend of $1.8 \pm 0.4 \text{ m s}^{-1} \text{ yr}^{-1}$ (Fig. C4) is indicative of a possible long-period companion, but a much longer observational baseline is needed to explore this. The sequence of period ratios close to 2 for the inner three planets may hint at an additional undiscovered planet exterior to planet d. Sub-Earth mass planets in periods longer than 20 d are below the current detection threshold, but could be revealed with further high precision RV measurements.

ACKNOWLEDGEMENTS

S.D., S.J., A.R., L.S., and M.Z. acknowledge support from the Deutsche Forschungsgemeinschaft under Research Unit FOR2544 “Blue Planets around Red Stars”, project no. DR 281/32-1. S.J. acknowledges project JE 701/3-1 and DFG priority program SPP 1992 “Exploring the Diversity of Extrasolar Planets” (RE 1664/18). E.R., C.R.-L., M.J.L.-G. and N.M. acknowledge financial support from the Spanish Agencia Estatal de Investigación through projects AYA2016-79425-C3-3-P, ESP2017-87676-C5-2-R, ESP2017-87143-R and the Centre of Excellence “Severo Ochoa” Instituto de Astrofísica de Andalucía (SEV-2017-0709). J.R.B. and C.A.H. are supported by STFC under grant ST/P000584/1. Z.M.B. acknowledges CONICYT-FONDECYT/Chile Postdoctorado 3180405. E.P. and I.R. acknowledge support from the Spanish Ministry for Science, Innovation and Universities (MCIU) and the Fondo Europeo de Desarrollo Regional (FEDER) through grants ESP2016-80435-C2-1-R and ESP2016-80435-C2-2-R, as well as the support of the Generalitat de Catalunya/CERCA programme. G.A.-E. research is supported by STFC Consolidated Grant ST/P000592/1.

Data were partly obtained with the MONET/South telescope of the MONitoring NETwork of Telescopes, funded by the Alfried Krupp von Bohlen und Halbach Foundation, Essen, and operated by the Georg-August-Universität Göttingen, the McDonald Observatory of the University of Texas at Austin, and the South African Astronomical Observatory. Data were partly collected with the robotic 40-cm telescope ASH2 at the SPACEOBS observatory (San Pedro de Atacama, Chile) operated by the Instituto de Astrofísica de Andalucía (IAA). We acknowledge the effort of various pro-am to obtain photometric monitoring during the Red Dots 2018 campaign through the AAVSO.

REFERENCES

- Alibert Y., Benz W., 2017, *A&A*, **598**, L5
 Anglada-Escudé G., Butler R. P., 2012, *ApJS*, **200**, 15
 Anglada-Escudé G., et al., 2016, *Nature*, **536**, 437
 Astudillo-Defru N., Delfosse X., Bonfils X., Forveille T., Lovis C., Rameau J., 2017a, *A&A*, **600**, A13
 Astudillo-Defru N., et al., 2017b, *A&A*, **602**, A88
 Astudillo-Defru N., et al., 2017c, *A&A*, **605**, L11
 Avenhaus H., Schmid H. M., Meyer M. R., 2012, *A&A*, **548**, A105
 Baluev R. V., 2009, *MNRAS*, **393**, 969
 Barnes J. R., et al., 2014, *MNRAS*, **439**, 3094
 Barnes J. R., Jeffers S. V., Haswell C. A., Jones H. R. A., Shulyak D., Pavlenko Y. V., Jenkins J. S., 2017, *MNRAS*, **471**, 811
 Berta Z. K., Irwin J., Charbonneau D., Burke C. J., Falco E. E., 2012, *AJ*, **144**, 145
 Bixel A., Apai D., 2017, *ApJ*, **836**, L31
 Boro Saikia S., et al., 2018, *A&A*, **616**, A108
 Butler R. P., et al., 2017, *AJ*, **153**, 208
 Chambers J. E., 1999, *MNRAS*, **304**, 793
 Coleman G. A. L., Nelson R. P., Paardekooper S. J., Dreizler S., Giesers B., Anglada-Escudé G., 2017, *MNRAS*, **467**, 996
 Coleman G. A. L., Leleu A., Alibert Y., Benz W., 2019, arXiv e-prints, p. [arXiv:1908.04166](https://arxiv.org/abs/1908.04166)
 Damasso M., Del Sordo F., 2017, *A&A*, **599**, A126
 Foreman-Mackey D., 2016, *The Journal of Open Source Software*, **24**
 Foreman-Mackey D., Hogg D. W., Lang D., Goodman J., 2013, *PASP*, **125**, 306
 Foreman-Mackey D., Agol E., Ambikasaran S., Angus R., 2017, *AJ*, **154**, 220
 Gaia Collaboration et al., 2018, *A&A*, **616**, A1
 Gaidos E., et al., 2014, *MNRAS*, **443**, 2561
 Gillon M., et al., 2017, *Nature*, **542**, 456
 Grimm S. L., et al., 2018, *A&A*, **613**, A68
 Hamsch F.-J., 2012, Society for Astronomical Sciences Annual Symposium, **31**, 75
 Henry T. J., Walkowicz L. M., Barto T. C., Golimowski D. A., 2002, *AJ*, **123**, 2002
 Jeffers S. V., et al., 2018a, *A&A*, **614**, A76
 Jeffers S. V., et al., 2018b, *A&A*, **614**, A76
 Kochanek C. S., et al., 2017, *PASP*, **129**, 104502
 Kopparapu R. K., Ramirez R. M., SchottelKotte J., Kasting J. F., Domagal-Goldman S., Eymet V., 2014, *ApJ*, **787**, L29
 Lo Curto G., et al., 2015, *The Messenger*, **162**, 9
 Luque R., et al., 2019, arXiv e-prints, p. [arXiv:1904.12818](https://arxiv.org/abs/1904.12818)
 Mayor M., et al., 2003, *The Messenger*, **114**, 20
 Meschiari S., Wolf A. S., Rivera E., Laughlin G., Vogt S., Butler P., 2009, *PASP*, **121**, 1016
 Mortier A., Collier Cameron A., 2017, *A&A*, **601**, A110
 Mortier A., Faria J. P., Correia C. M., Santerne A., Santos N. C., 2015, *A&A*, **573**, A101
 Neves V., Bonfils X., Santos N. C., Delfosse X., Forveille T., Alard F., Udry S., 2014, *A&A*, **568**, A121
 Newton E. R., Irwin J., Charbonneau D., Berlind P., Calkins M. L., Mink J., 2017, *ApJ*, **834**, 85
 Pizzoloto N., Maggio A., Micela G., Sciortino S., Ventura P., 2003, *A&A*, **397**, 147
 Reiners A., Joshi N., Goldman B., 2012, *AJ*, **143**, 93
 Reiners A., Schüssler M., Passegger V. M., 2014, *ApJ*, **794**, 144
 Ribas I., et al., 2018, *Nature*, **563**, 365
 Ricker G. R., et al., 2015a, *Journal of Astronomical Telescopes, Instruments, and Systems*, **1**, 014003
 Ricker G. R., et al., 2015b, *Journal of Astronomical Telescopes, Instruments, and Systems*, **1**, 014003
 Rivera E. J., Laughlin G., Butler R. P., Vogt S. S., Haghighipour N., Meschiari S., 2010, *ApJ*, **719**, 890
 Rodgers A. W., Eggen O. J., 1974, *PASP*, **86**, 742
 Rodriguez D. R., Duchêne G., Tom H., Kennedy G. M., Matthews B., Greaves J., Butner H., 2015, *MNRAS*, **449**, 3160
 Schmitt J. H. M. M., Liefke C., 2004, *A&A*, **417**, 651
 Skrutskie M. F., et al., 2006, *AJ*, **131**, 1163
 Stassun K. G., et al., 2018, *AJ*, **156**, 102
 Suárez Mascareño A., Rebolo R., González Hernández J. I., Esposito M., 2015, *MNRAS*, **452**, 2745
 West A. A., Hawley S. L., Bochanski J. J., Covey K. R., Reid I. N., Dhital S., Hilton E. J., Masuda M., 2008, *AJ*, **135**, 785
 Wright N. J., Drake J. J., Mamajek E. E., Henry G. W., 2011, *ApJ*, **743**, 48
 Wright D. J., Wittenmyer R. A., Tinney C. G., Bentley J. S., Zhao J., 2016, *ApJ*, **817**, L20
 Zechmeister M., Kürster M., 2009, *A&A*, **496**, 577
 Zechmeister M., et al., 2018, *A&A*, **609**, A12
 Zechmeister M., et al., 2019, *A&A*, **627**, A49
 Zeng L., Sasselov D. D., Jacobsen S. B., 2016, *ApJ*, **819**, 127

Table A1. HARPS pre-upgrade, pre-Red Dots data obtained by *SERVAL*.

BJD	RV [m/s]	σ_{RV} [m/s]
2452985.714000	-35.96	1.82
2452996.738000	-25.68	2.64
2453337.750000	-42.07	1.64
2454341.869000	-15.33	2.04
2455545.668000	-33.95	1.63
2455612.524000	-13.61	1.83
2455998.513000	-9.65	1.72

Table A2. HARPS post-upgrade data obtained by *TERRA* and *SERVAL* (dLW). Outliers are flagged (RV or dLW) in the last column. Data are given in 1-day averages and 1 m/s has been quadratically added to the RV uncertainties. Full table in online data.

BJD	RV [m/s]	σ_{RV} [m/s]	dLW [m ² /s ²]	σ_{dLW} [m ² /s ²]	flag
2458020.814834	1.48	1.69	-12.1	3.6	
2458040.854023	-6.77	1.06	2.9	1.4	
2458043.783336	2.56	1.66	0.9	1.4	
2458052.765154	-1.54	1.59	2.6	1.4	
2458053.866459	-6.16	1.05	7.7	1.4	
2458054.699823	-7.11	1.26	-0.3	1.2	

APPENDIX A: RADIAL VELOCITY DATA

In Table A1 and A2 we list the all radial velocity data for GJ 1061. Radial velocities are obtained using *SERVAL* and *TERRA*. Note that the full Table A2 is available online.

APPENDIX B: MODELING DETAILS

We start our *python*-based detailed analysis using *scipy.optimize.minimize*. For each Keplerian signal we use the parameters provided from the GLS analysis as starting values (amplitude, period, periastron time). The best fit and its uncertainties are used to then initialize the MCMC run with 500 walkers and 3000 steps. As priors for all parameters, we use a normal distribution with the best fit as mean and 100 times the uncertainty as the standard deviation. After the run we check that the parameter distribution was not affected by the initialisation. Boundaries are set only for numerical reasons, e.g. to avoid numerical problems with too large or too small values for the kernel parameters. To avoid non-physical parameter combinations, the absolute value of the eccentricity is used when calculating the Keplerian models. The absolute value of the velocity amplitude is used in order to avoid degenerate solutions. In case the final best solution from the MCMC chains is significantly better than the starting parameters, this procedure is repeated with the new best parameter set.

The correlation of the data is modeled using the Gaussian Process Regression framework. We use the *celerite* package (Foreman-Mackey et al. 2017) since it only scales linearly with the number of data points and not cubical. The *REAL* kernel of *celerite* represents an exponential decaying coher-

ence of the data and has two parameters, the amplitude a and the inverse damping time scale c (to avoid negative values for a and c , the logarithm of the values are used):

$$k(\tau) = a e^{-c\tau}$$

The *SHO* kernel represents a stochastically driven, damped harmonic oscillator. It is defined through its power spectral density (PSD) using three parameters, an amplitude S_0 , the quality factor Q describing the damping and the oscillator frequency ω_0 . Like in the *REAL* kernel, the logarithms of the parameters are used. The quality factor is related to the inverse of the damping time. The PSD of this term is:

$$S(\omega) = \sqrt{\frac{2}{\pi}} \frac{S_0 \omega_0^4}{(\omega^2 - \omega_0^2)^2 + \omega_0^2 \omega^2 / Q^2}$$

APPENDIX C: MCMC CORNER PLOTS

We show the posterior distribution from 500 walkers and 30 000 steps (the first half rejected as burn-in) are as corner plots using *corner* (Foreman-Mackey 2016) in Figs. C1 to C4, first for the full fit parameter set and then parameter subsets for the individual planets (Figs. C2 and C3) as well as for instrumental parameters (Fig. C4). For the parameter subsets we show absolute values for the eccentricities, the longitude of periastron and the periastron passage time are converted modulo 2π and orbital period, respectively. The subset corner plots also contain derived parameters, i.e. the semi-major axis, the planetary minimum mass as well as the longitude of periastron. For the former two we propagate the uncertainties in the stellar mass. The 4th signal is modeled using the *SHO*-kernel.

APPENDIX D: PERIODOGRAMS

The subsequent subtraction of Keplerian signals from the radial velocity data is shown in Fig. 1 as GLS-periodograms (Zechmeister & Kürster 2009). In addition, the periodograms of the signals are shown in Fig. D1.

We also use the Stacked Bayesian Generalized Lomb-Scargle (SBGLS) periodogram (Mortier et al. 2015; Mortier & Collier Cameron 2017) in order to check the development of the signals with increasing number of data points (Fig. D2). The three planetary signals are indeed stable in period and their probability is increasing with the number of data points as expected for coherent signals.

APPENDIX E: PHOTOMETRY

The used photometric facilities are summarized in Table E1. They are:

ASH2. The ASH2 (Astrograph for South Hemisphere II) telescope) is a robotic 40 cm telescope with a CCD camera STL11000 2.7k×4k, FOV 54×82 arcmin². The telescope is at SPACEOBS¹² (San Pedro de Atacama Celestial Explorations Observatory), at 2450 m above the sea, located in the northern Atacama Desert in Chile. During the present

¹² <http://www.spaceobs.com/en>

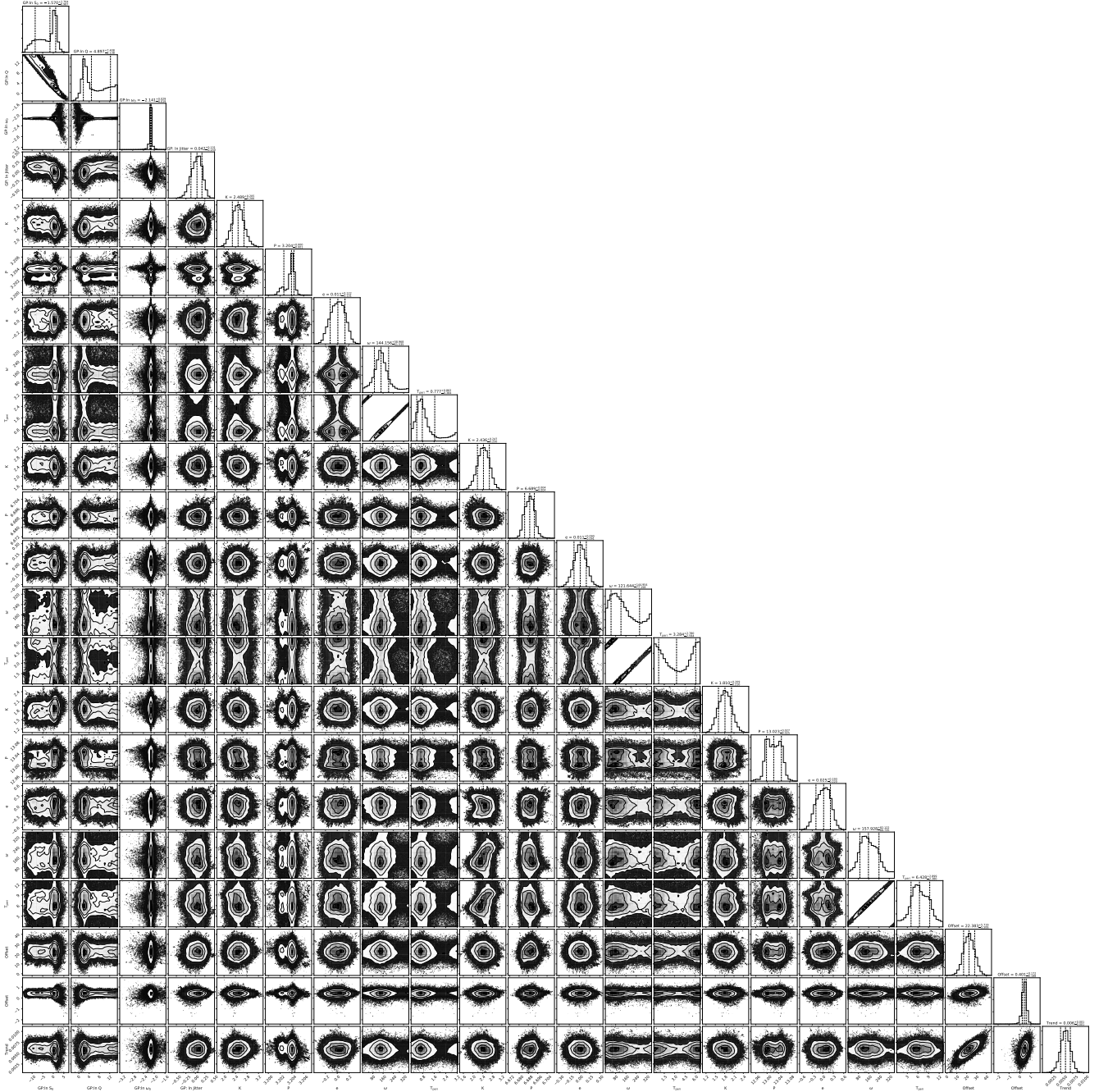


Figure C1. MCMC posterior distribution of full parameter set for the 3-Keplerian signals plus *SHO* model.

work, only subframes with 40% of the total FOV were used, resulting in a useful FOV of 21.6×32.8 arcmin². Data are obtained as differential magnitude relative to a main reference star. A set of five check stars were selected and used for checking purposes. In total, 32 epochs in V and R bands were obtained in the period between July and October, 2018, with a time span of 97 days.

MONET-S. The 1.2 m MONET-South¹³ telescope (MONitoring NETwork of Telescopes) is located at the SAAO

(South African Astronomical Observatory), South Africa. It is equipped with a Finger Lakes ProLine 2k \times 2k e2v CCD, FOV 12.6×12.6 arcmin². We performed aperture photometry with the AstroImageJ package using a set of about five comparison stars. 43 epochs in the R band were collected during the Red Dots campaign.

AAVSO. Within the AAVSO collaboration, the Remote Observatory Atacama Desert (ROAD) (Hambusch 2012) was used. This is also located at SPACEOBS. It is equipped with a 40 cm f/6.8 Optimized Dall-Kirkham (ODK) reflector from Orion Optics, UK, and a CCD camera ML16803 4k \times 4k from

¹³ <https://monet.uni-goettingen.de/>

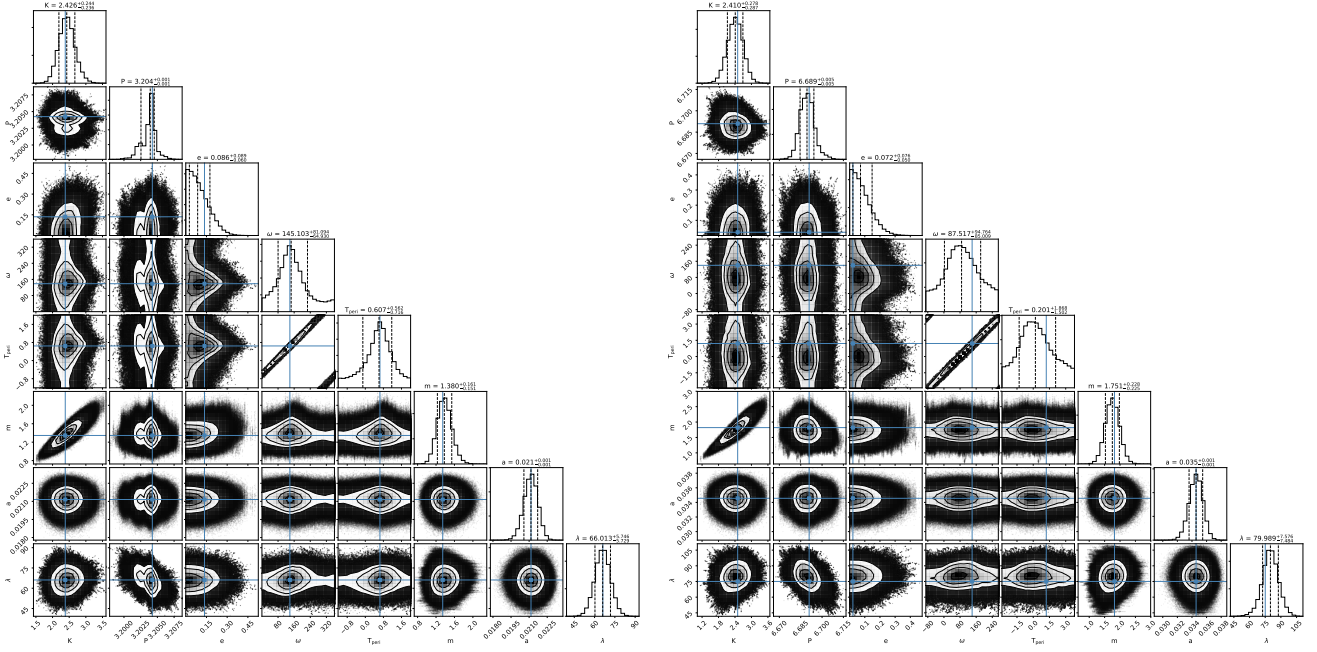


Figure C2. MCMC posterior distribution for Keplerian parameters of planet b and c.

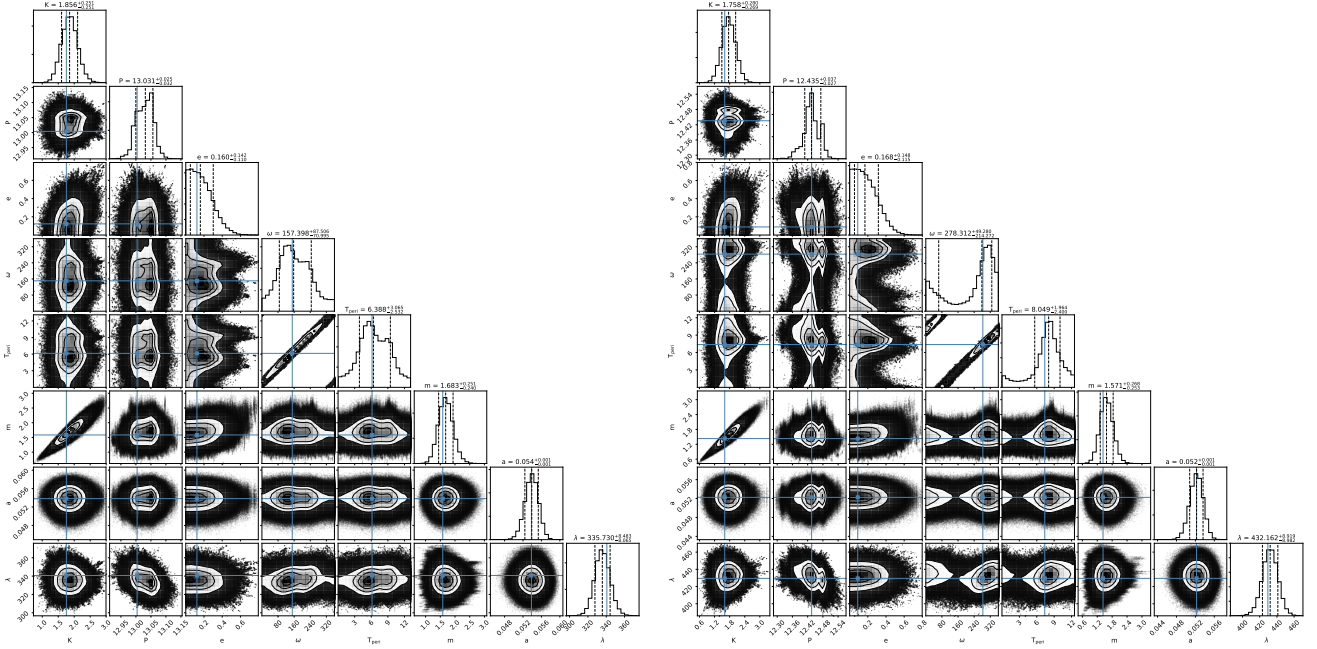


Figure C3. Same as Fig. C2 but for planet d choosing 13.0 and 12.4 d period.

FLI, USA, equipped with Astrodon UBVRi photometric filters. Data were reduced using the LesvePhotometry package with two comparison stars, one for reference and another one for checking purposes. These observations were also collected simultaneously with the Red Dots campaign.

TESS. At the end of Red Dots campaign, GJ 1061 was also observed by the TESS¹⁴ satellite (Ricker et al. 2015b).

This was carried out during two consecutive sectors of 27 days each, with a effective total time span of about 53 days between September and November 2018, with the main aim of investigating possible transit signals.

MEarth-S. The MEarth project¹⁵ consists of two robotically controlled observatories dedicated to monitoring thousands of M-dwarf stars (Berta et al. 2012): MEarth-N

¹⁴ <http://heasarc.gsfc.nasa.gov/docs/tess/>

¹⁵ <https://www.cfa.harvard.edu/MEarth/>

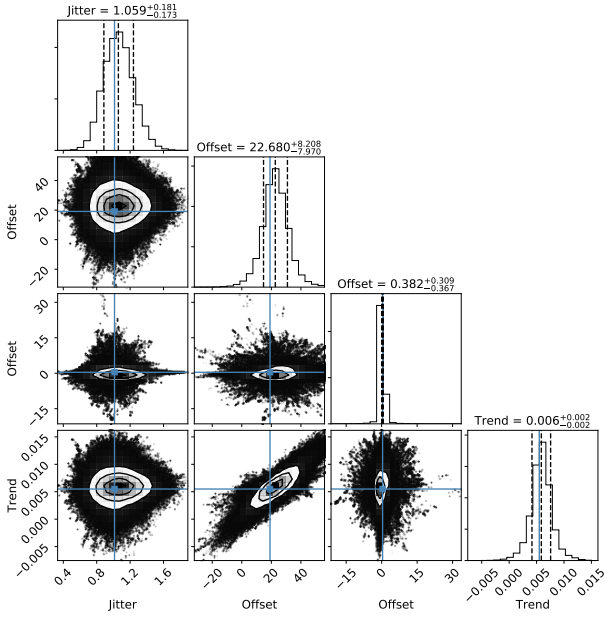


Figure C4. *Left:* MCMC posterior distribution for $\ln(\text{jitter})$, offsets, and trend parameters. *Right:* Parameter for the *SHO* kernel.

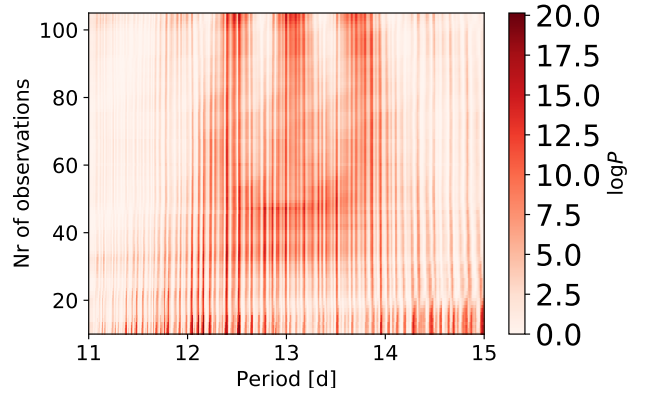
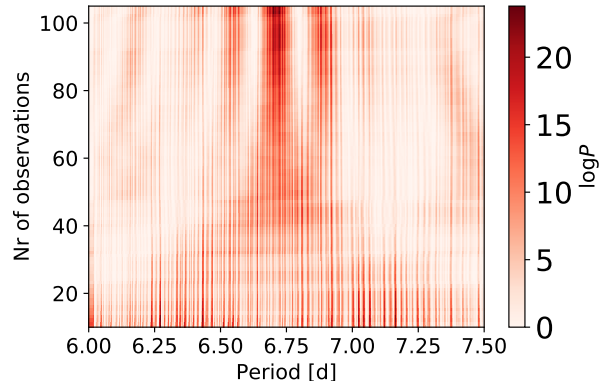
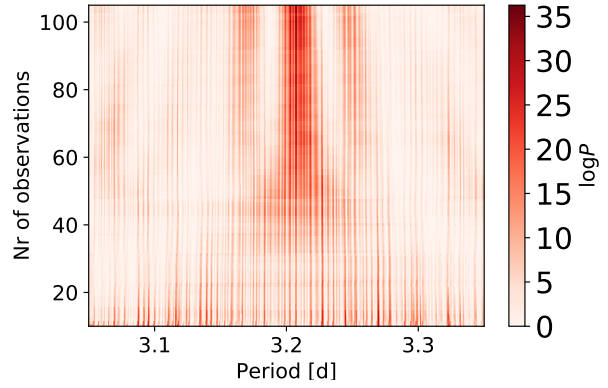


Figure D2. SBGLS periodograms zoomed around the 3.204 d period (top) and subsequent removal of the 3.204 d (middle) as well as the 6.689 d signal (bottom). The number of observations is plotted against period, with the colour scale indicating the logarithm of the probability, where darker is more likely.

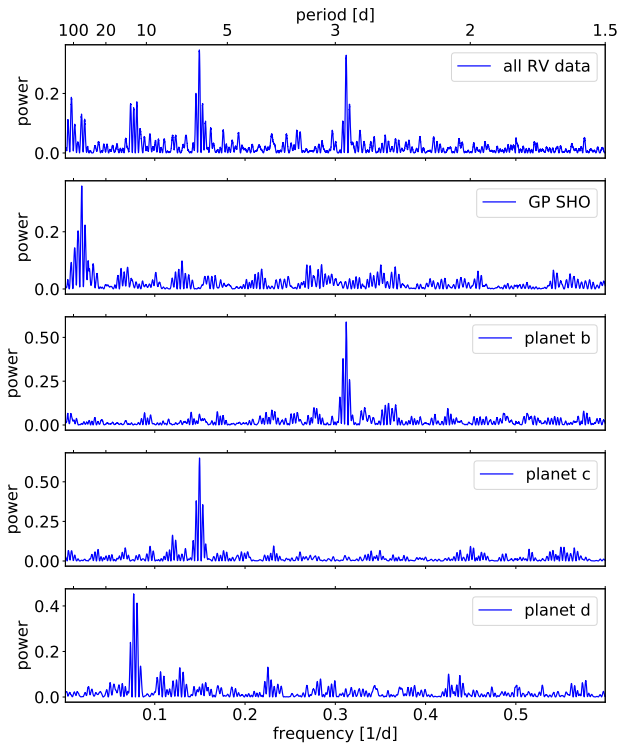


Figure D1. Periodograms of all observation (top) and models.

(North), at Fred Lawrence Whipple Observatory (FLWO), USA, since 2008 and M_{Earth}-S (South), at Cerro Tololo Inter-American Observatory (CTIO), Chile, since 2014. Each array consists of eight identical 40 cm robotic telescopes ($f/9$ Ritchey-Chrétien Cassegrain), each equipped with a $2k \times 2k$ CCD camera, FOV 26×26 arcmin², sensitive to red optical and near-infrared light. M_{Earth} project generally uses an RG715 long-pass filter, except for the 2010-2011 season when an $I_{715-895}$ interference filter was chosen. In the case of GJ 1061, two time series are available from the

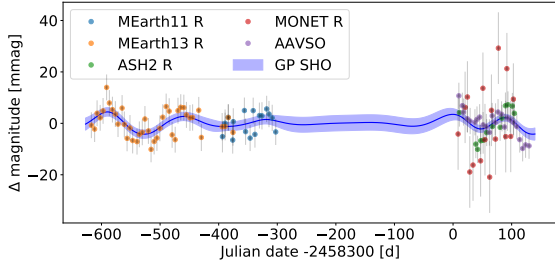


Figure E1. Photometric data, shown in five day bins together with a stochastically driven, damped harmonic oscillator model using the *SHO* kernel with 130 d period and 20 d damping time.

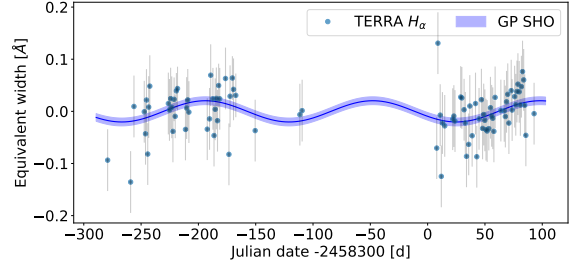


Figure F1. $H\alpha$ data, shown with a stochastically driven, damped harmonic oscillator model using the *SHO* kernel with 130 d period and 20 d damping time.

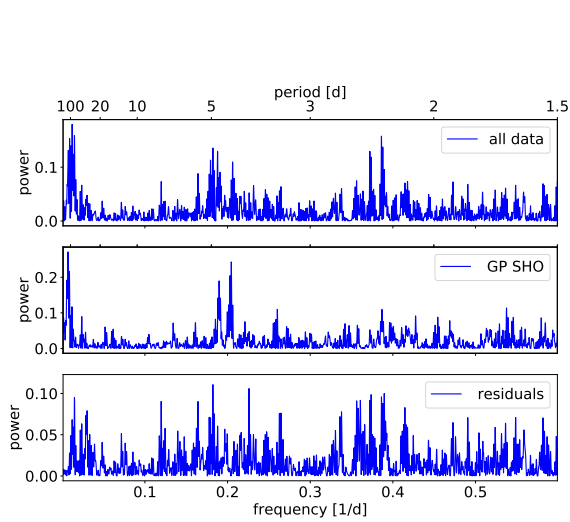


Figure E2. Periodogram of photometric data (top), of the *SHO* kernel (middle) and of the residuals (bottom).

MEarth-S project, which have been collected with telescopes number 11 (T11) (year 2017) and 13 (T13) (2016-2017).

ASAS-SN. The ASAS-SN project¹⁶ (All-Sky Automated Survey for Supernovae) (Kochanek et al. 2017) currently consists of 24 telescopes distributed on 6 units around the Globe, located in Hawaii (Haleakala Observatory), Chile (CTIO, 2 units), Texas (McDonald Observatory), South Africa (SAAO) and China. Each station consists of four 14 cm aperture Nikon telephoto lenses, each with a thermoelectrically cooled, back-illuminated, 2k×2k, Finger Lakes Instruments, ProLine CCD camera. The field of view of each camera is roughly 4.5 deg² with a pixel scale of 8.0 arcsec.

The combined photometric data are listed in Table E2 and shown in Fig. E1 together with a model using the *SHO*-kernel from *celerite*. The signal at about 130 d is well described with this quasi-periodic oscillations as visible from the periodograms in Fig. E2. The analysis is presented in the main text in Sect. 4.2.2.

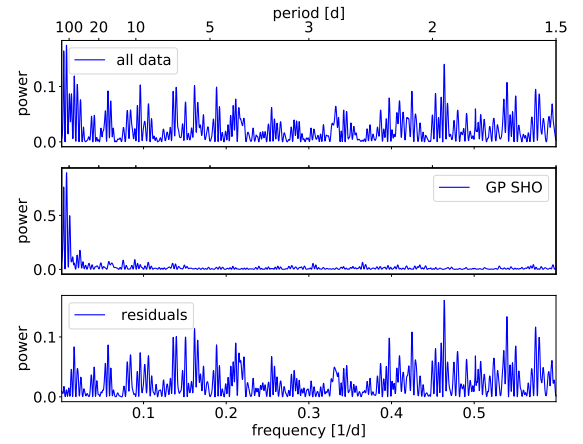


Figure F2. Periodogram of $H\alpha$ data (top), of the *SHO* kernel (middle) and of the residuals (bottom).

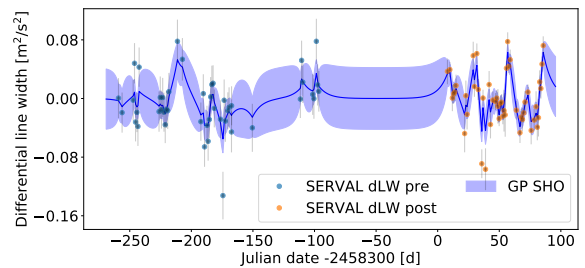


Figure F3. Differential line width data, shown together using the *REAL* kernel with 3.5 d decay time.

APPENDIX F: ACTIVITY INDICATORS

TERRA and *SERVAL* provide various spectroscopic activity indicators, among those the $H\alpha$ as well as NaD equivalent width and the differential line width. These measurements are listed in Tables F1 and A2. The spectroscopic activity indicators have been investigated for signals with periods at

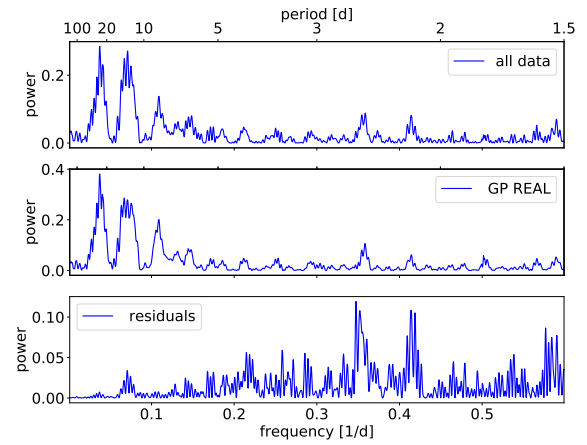
¹⁶ <http://www.astronomy.ohio-state.edu/asassn/>

Table E1. Photometric observing facilities.

Acronym	Location	Tel (m)	FOV (arcmin ²)	CCD	Scale (arcsec pix ⁻¹)	Band(s)
ASH2	SPACEOBS, Chile	0.40	54.0×82.0	2.7k×4k	1.20	V,R
MONET-S	SAAO, South Africa	1.20	12.6×12.6	2k×2k	0.37	R
AAVSO	SPACEOBS, Chile	0.40	47×47	4k×4k	0.69	V
TESS	TESS satellite	4×0.105	4×(24°×24°)	4k×4k	21.1	TESS
MEarth-S	CTIO, Chile	0.40	26.0×26.0	2k×2k	0.76	RG715
ASAS-SN	worldwide	4×0.14	4.5 deg ²	2k×2k	8.0	V

Table E2. Ground-based photometry, full table in online data.

BJD	rel. mag	σ rel. mag
ASH2 R		
2458309.830903	0.0062	0.0016
2458310.834277	0.0048	0.0024
ASH2 V		
2458309.829251	0.0001	0.0020
2458310.835848	0.0028	0.0040
MONET-S R		
2458308.622806	0.0022	0.0010
2458318.563727	0.0160	0.0011
AAVSO R		
2458308.901969	0.0119	0.0017
2458309.899256	0.0137	0.0015
MEarth RG715		
2457905.943122	-0.0043	0.0029
2457906.939185	-0.0067	0.0073

**Figure F4.** Periodogram of differential line width data (top), of the *REAL* kernel (middle) and of the residuals (bottom).**Table F1.** Equivalent widths obtained by *TERRA* in the HARPS post-upgrade, data. The flag 0 indicates rejected data due to possible flares. Full table in online data.

BJD	H α Å	Na D1 Å	Na D2 Å	flag
2458020.814834	-0.12	1.17	0.95	1
2458040.854023	-0.16	1.17	0.90	1
2458043.783336	-0.02	1.23	0.97	1
2458052.765154	-0.03	1.18	0.93	1

the potential planetary periods to avoid false positive planet detections as well as for the detection of the stellar rotation. In Fig. F3 we show the fit of the differential line width, in Fig. F1 for the H α equivalent width. The periodograms of the data, signals and residuals are shown in Figs. F4 and F2. The analysis is presented in the main text in Sect. 4.2.1.

This paper has been typeset from a $\text{\TeX}/\text{\LaTeX}$ file prepared by the author.